2.5 THE EFFECT OF CLIMATE ON INTER-ANNUAL VARIABILITY OF TERRESTRIAL CO_2 FLUXES

Kevin Schaefer[1], A. Scott Denning[1], Neil Suits[1], Jörg Kaduk[2], Ian Baker[1], Sietse Los[3], Lara Prihodko[1]
[1]Department of Atmospheric Science, Colorado State University, Fort Collins, Colorado

[2]Department of Geography, University of Leicester, Leicester LE1 7RH, United Kingdom

[3]Department of Geography, University of Wales, Swansea, United Kingdom

1. Introduction

The measured atmospheric CO_2 growth rate is half that expected based on fossil fuel emissions. Modeling, isotope, and inversion studies place mu[1]ch of this "missing sink" in the northern hemisphere terrestrial biosphere. The global, atmospheric CO_2 growth rate shows a great deal of inter-annual variability [*Conway et al*., 1994; *LLoyd*, 1999; *Rayner and Law*, 1999; *Tans and Wallace*, 1999; *Bousquet et al*., 2000; *Fung*, 2000]. The ocean fluxes show relatively low variability [*Rayner and Law*, 1999, *Le Quéré et al*., 2000], so growth rate variability is attributed primarily to changes in the terrestrial sink [*Sarmiento*, 1993, *Conway et al*., 1994; *Trolier et al*., 1996; *Kaduk and Heimann*, 1997; *LLoyd*, 1999; *Houghton et al*., 1998; *Tans and Wallace*, 1999; *Houghton*, 2000; *Prince et al*., 2000]. Climate, land use change, natural disturbance, CO_2 fertilization, and nitrogen deposition all affect terrestrial CO_2 fluxes [*Conway et al*., 1994; *Bousquet et al*., 2000, *Fung*, 2000, *Houghton*, 2000]. Climate is most important [*Houghton*, 2000], but how precipitation, temperature, and other climate factors control net terrestrial CO_2 fluxes is unclear.

Net Ecosystem Exchange (NEE) is the net CO_2 flux from the terrestrial biosphere:

$$NEE = R - GPP \,, \qquad (2)$$

where R is respiration, and GPP is gross primary production or photosynthesis. Photosynthesis removes CO_2 from the atmosphere and respiration returns CO_2 to the atmosphere. A positive NEE indicates a net CO_2 flux into the atmosphere. Breaking R into autotrophic and heterotrophic respiration gives

$$NEE = R_H + R_R + R_C - GPP \,, \qquad (3)$$

where R_H is heterotrophic respiration, R_R is root autotrophic respiration, and R_C is canopy autotrophic respiration. Heterotrophic respiration is the decay of organic material by microorganisms. Autotrophic respiration is the release of CO_2 during plant maintenance and growth. Combining terms gives

$$NEE = R_g - A_n \,. \qquad (4)$$

where $R_g = R_H + R_R$ is ground respiration and $A_n = GPP - R_C$ is canopy net photosynthesis. R_g depends on soil temperature, soil moisture, and the mass of carbon in the soil [*Parton et al.*, 1993; *Raich et al.*, 1991; *Hunt et al.*, 1996; *Sitch et al.*, 2000]. A_n is resource-limited by Rubisco (nitrogen) availability, available light, or leaf export capacity. A_n depends on soil moisture, canopy temperature, humidity, and the number of leaves (i.e., LAI) [*Sellers et al*., 1996a,b].

Lacking direct measurements, we estimate global NEE from satellite data, inversions, and models. Satellite data, e.g., the Normalized Difference Vegetation Index (NDVI), is used to estimate photosynthesis [*Ichii et al*., 2001], but does not contain information on respiration. Inversions can estimate NEE for continental scale regions, but cannot isolate exact causes of variability [e.g., *Bousquet et al*., 2000]. Terrestrial carbon models suggest precipitation and temperature influence NEE inter-annual variability, but disagree because of differences in how explicitly they represent photosynthesis and respiration processes [*Kaduk and Heimann*, 1997; *LLoyd*, 1999; *Dickinson*, 2000; *Houghton*, 2000]. We used detailed plant photosynthesis and respiration models to 1) quantify how climate influences NEE inter-annual variability, 2) explain regional and ecosystem differences, and 3) explain the effects of phenomena known to affect precipitation and temperature.

2. Methods

We used the Simple Biosphere model, Version 2 (SiB2) to estimate NEE for 1983 to 1993 on a global, 1° by 1° grid with a 10-minute time step [*Sellers et al*., 1996a]. We investigated the effects of climate only and did not consider variability due to ocean uptake, fossil fuel emissions, land use, CO_2 fertilization, natural disturbances, or nitrogen deposition.

SiB2 has high time resolution and detailed plant physiology to isolate the long-term influences of climate factors with strong diurnal variability, such as precipitation and temperature. SiB2 uses the *Farquahar et al*. [1981] photosynthesis model scaled to the canopy level [*Sellers et al*., 1996a], the Ball-Berry-Collatz stomatal conductance model [*Ball*, 1988, *Collatz et al*., 1991, 1992], and the respiration model of *Denning et al*. [1996]. SiB2 accounts for the effects of snow cover,

---

Corresponding author address: Kevin Schaefer, Colorado State University, Department of Atmospheric Sciences, Fort Collins, CO 80523-1371, email: kevin@atmos.colostate.edu rainfall interception by the canopy, and aerodynamic turbulence [*Sellers et al*., 1996a].

As input, SiB2 requires Leaf Area Index (LAI), vegetation cover fraction, vegetation type, soil type, and weather data. We estimated LAI using global, 1° by 1° composite maps of NDVI adjusted for missing data, satellite orbit drift, differing instrument calibrations, sensor degradation, and volcanic aerosols [*Sellers et al*., 1994a; *Los et al*., 1998; *Los et al*., 1999]. The vegetation characteristics and soil types came from *Sellers et al*. [1996b]. We used the *DeFries and Townshend* [1994] global map of 11 vegetation types. We estimated vegetation cover fraction using the *Los et al*. [2000] method, but used the peak NDVI value for the entire 11-year period.

Weather data came from the European Centre for Medium-range Weather Forecasts (ECMWF) Reanalysis [*Gibson et al*., 1999]. ECMWF Reanalysis contains surface temperature, pressure, wind speed, precipitation, and radiation data every 6 hours. Except for the incident sunlight, the ECMWF data was linearly interpolated between data points. The sunlight was scaled by the cosine of the solar zenith angle to assure no light falls on the canopy at night while conserving energy. ECMWF data were available for 1978 through 1993 and NDVI data for 1983 through 1999, limiting this study to 1983 through 1993.

To calculate R_g, we adapted the respiration model of *Denning et al.* [1996a]:

$$R_g = R^* R_f \,, \quad (5)$$

where R^* is a combined soil temperature and moisture scaling factor and R_f is the respiration factor. R_g increases exponentially with soil temperature [*Raich and Schlesinger*, 1992]. R_g increases with soil moisture to an optimum value then decreases (too much water limits the oxygen available to microbes) [*Raich et al*, 1991]. The optimal soil moisture, W_{opt} varies between 0.6 and 0.7, depending on soil type.

We assumed A_n and R_g balance with a 1-year turnover time: carbon accumulated by photosynthesis is released via respiration over a period of one year. This assures a balanced carbon cycle, but allows perturbations in photosynthesis in one year to affect respiration the following year. R_f is the respiration rate that balances A_n when adjusted for soil temperature and water content:

$$R_f = \frac{\sum_{\text{1 year}} A_n}{\sum_{\text{1 year}} R^*} \,. \qquad (6)$$

We distribute the Accumulated carbon in the soil based on root density profiles that decrease exponentially with soil depth [*Jackson et al*., 1996]. We calculated a "rolling" R_f each month based on the previous 12 months of A_n and R^*.

Precipitation, temperature, relative humidity, sunlight, and available biomass all influence NEE. We grouped these factors into those that effect *GPP* and those that effect *R* (Table 1). Precipitation and temperature appear twice because they affect both. These variables change with the ECMWF weather data (which represents boundary layer values above the canopy), but also respond to changes in *GPP* and *R* and depend on the physical characteristics of the canopy and soil. LAI represents above ground biomass and the rolling R_f represents variations in soil carbon. The influence of precipitation on *GPP* is limited to root zone soil moisture stress (i.e., drought stress).

Table 1. Climate factors, SiB2 variables, and associated reference values

Climate Factor	Group	SiB2 Variable	Reference Value
Humidity	*GPP*	Leaf surface relative humidity	1.0
Light	*GPP*	Sunlight incident on canopy top	200 W m^{-2}
Leaf Area Index	*GPP*	Leaf Area Index	LAI_{max}
Temperature	*GPP*	Canopy temperature	298.15 K
Precipitation	*GPP*	Root zone soil water fraction	1.0
Temperature	*R*	Root zone soil temperature	298 K
Precipitation	*R*	Root zone soil water fraction	W_{opt}
Soil Carbon	*R*	Respiration factor	R_{fmean}

To quantify climate influences on NEE variability, we calculated reference rates for *GPP* and *R* for each climate variable and compared them to the actual rate:

$$E_i = \left|GPP_i - GPP\right| \text{ or } E_i = \left|R_i - R\right| \qquad (7)$$

where E_i is the influence and GPP_i and R_i are reference rates for the i^{th} climate variable. The absolute value ensures non-negative monthly averages of E_i. All E_i were calculated each time step and have units of flux. When a variable does not influence NEE, $E_i = 0$. For example, precipitation variability only affects GPP when the soil gets too dry (i.e., drought stress).

To calculate the reference rate (GPP_i or R_i), we kept all inputs the same and changed the i^{th} climate factor to a reference value as listed in Table 1. As humidity decreases, stomata close to minimize water loss (i.e., humidity stress), so we chose the optimal humidity value of 1.0. For LAI, we chose the maximum LAI for each biome [*Sellers et al*., 1996b]. For precipitation influence on *GPP*, we chose fully saturated soil ($W = 1.0$). For precipitation influence on *R*, we chose the optimal soil water content for maximum heterotrophic respiration, W_{opt} [*Raich et al*., 1995]. For temperature influence on *GPP* and *R*, we chose reference values from *Sellers et al*. [1996a]. For sunlight we chose a typical saturated value (the canopy usually absorbs more light than it uses for photosynthesis). For soil carbon, we chose an average respiration factor for all months, R_{fmean}.

To assure E_i scales properly with *GPP* or *R*, (i.e., E_i is small when *GPP* is small and large when *GPP* is large), we calculated weighted monthly averages:

$$\overline{E_i} = \frac{\overline{GPP \cdot E_i}}{\overline{GPP}} \text{ or } \overline{E_i} = \frac{\overline{R \cdot E_i}}{\overline{R}} , \qquad (8)$$

where the overbar represents a monthly average. We calculated mean seasonal variations from global maps of monthly averages by averaging all Januaries, Februaries, etc. This produced one global map for each month representing the seasonal variation. Subtracting seasonal variation maps from monthly average maps produced monthly anomaly maps:

$$X' = \overline{X} - \tilde{X} , \quad (9)$$

where X' is the monthly anomaly, $\overline{X}$ is the monthly mean, and $\tilde{X}$ is the seasonal variation of variable *X*. From anomaly maps, we produced maps of standard deviation, correlation, and other statistical parameters. Multiplying by grid cell area (which varies with latitude) and adding all land pixels produced total global land fluxes as a function of time.

3. NEE Variability

The northern hemisphere has more land and vegetation than the southern hemisphere and dominates the global NEE seasonal cycle (Figure 1). NEE is most strongly negative during the northern hemisphere summer when global GPP is greatest. NEE is most strongly positive in northern hemisphere fall when assimilation drops off and global R dominates. The secondary minimum in November results from the surge in global GPP in the southern hemisphere spring. The NEE averages to zero over many years. However, small changes in GPP and R each year result in inter-annual NEE variability of about ± 2 GtC year^{-1}.

The simulated global NEE anomalies agree fairly well with the measured global CO_2 growth rate (Figure 2) [*Conway et al.*, 1994], with estimates of *McGuire et al*. [2001] using biogeochemical models, *Bousquet et al*. [2000] with inversions of flask measurements using a transport model, and with the from the long-term Mona Loa record [*Kaduk and Heimann*, 1997]. Error in our simulated NEE may result from 1) NDVI interpolation over tropical forests to account for persistent cloud cover [*Los et al*., 2000], 2) assuming a uniform 1-year carbon turnover time for all biome types, 3) exclusion of ocean fluxes, 4) transport lag between surface fluxes and flask measurements, and 5) SiB2 approximations.

A map of NEE standard deviation (Figure 3) shows tropical grasslands have the highest variability followed by northern extra-tropical forests. Equatorial rain forests have fairly low variability except for the western half of the Amazon basin. The large South American anomaly results from precipitation variability from El Niño-Southern Oscillation (ENSO) and potential problems with the ECMWF precipitation data (see below). Although deserts are highly variable relative to their seasonal amplitude, low *GPP* results in low NEE standard deviations.

Variability in the Northern extra-tropics is not as spatially uniform as implied in Figure 3. A typical map of simulated NEE anomalies for July 1984 (Figure 4) shows a pattern of alternating positive and negative regions across the northern hemisphere. Anomaly amplitudes range from 0.2 to 0.4 GtC yr^{-1} with periods of 2-3 years. These regional anomalies tend to cancel, negating the effect of much greater land area in the northern hemisphere. While the northern hemisphere dominates the global NEE seasonal cycle, the tropics dominate global NEE inter-annual variability.

4. Climate Influences

NEE anomalies depend on the relative magnitude of *GPP* and *R* anomalies because both respond in similar ways to climate and tend to cancel each other. The relative magnitude of *GPP* and *R* variance measures their relative influence NEE variability:

$$f_{GPP} = \sigma^2_{GPP} \Big/ (\sigma^2_{GPP} + \sigma^2_R) \text{ and } f_R = \sigma^2_R \Big/ (\sigma^2_{GPP} + \sigma^2_R) , \qquad (10)$$

where f_{GPP} and f_R are relative influences, σ_{GPP} and σ_R are standard deviations, and σ^2_{GPP} and σ^2_R are variances of *GPP* and *R*. When $f_R = 0$, respiration has no influence on NEE inter-annual variability; when $f_R = 1$, respiration totally controls NEE variability (by definition, $f_{GPP} = 1 - f_R$).

R dominates NEE variability at high latitudes (Figure 5) while *GPP* and *R* exert roughly equal influences in the highly variable tropical grasslands. Although *GPP* variability almost totally controls the deserts, these regions have such low *GPP* they do not significantly affect global NEE inter-annual variability. Overall, *R* accounts for 59% and *GPP* for 41% of the global NEE inter-annual variability.

Climate variables do not vary independently of one another. For example, increasing canopy temperature increases *GPP*, but decreases relative humidity (which decreases *GPP*). Comparing relative magnitudes of $\overline{E_i}$ variance accounts for such cancellation. The total influence of the *GPP* group cannot exceed the relative influence of *GPP* itself such that

$$f_i = \frac{\sigma_i^2}{\sum \sigma_i^2} f_{GPP} \text{ or } f_i = \frac{\sigma_i^2}{\sum \sigma_i^2} f_R , \qquad (11)$$

where f_i is the relative influence of the i^{th} climate factor and σ_i^2 is the variance of $\overline{E_i}$. When $f_i = 0$, the climate factor has no influence and when $f_i = 1$, the climate factor totally controls NEE inter-annual variability. By definition, the sum of all f_i for both the *R* and *GPP* groups equals one ($\sum f_i = 1$). Maps of f_i show strong regional differences in the influence of climate on NEE variability (Figure 6).

Precipitation control of *GPP* (Figure 6a) and *R* (Figure 6b) dominate throughout the tropics. The *GPP* and *R* precipitation influence patterns do not significantly overlap. The demarcation lies roughly where the average soil moisture equals W_{opt}. This division is especially clear in regions with a strong spatial gradient in soil moisture (e.g., sub-Saharan Africa and South America). The soil moisture influence on *GPP* represents drought stress. In semi-arid and desert regions with drier soils ($W < W_{opt}$), precipitation control of *GPP* dominates because respiration can occur even in very dry soils while *GPP* ceases below minimum soil water content. In nearly saturated soils ($W > W_{opt}$), precipitation changes effect respiration, but do not induce drought stress, so precipitation control of *R* dominates.

The large NEE anomaly in South America (Figure 3) may result from problems with the ECMWF precipitation data as well as naturally occurring drought stress. Spatial patterns of precipitation differ between datasets derived from rain gauge data and those from reanalysis using a model [*Costa and Foley*, 1998]. The precipitation data from the ECMWF reanalysis is diagnostic and unconstrained by rain gauge measurements. The spectral representation of topography in ECMWF produces false undulations in the land surface, creating potentially suspect precipitation anomalies in South America [*Costa and Foley*, 1998]. Bright NDVI data may indicate plant growth, but the ECMWF may systematically put the rain somewhere else, resulting in drought stress.

Temperature influence on respiration dominates NEE variability at high latitudes (Figure 6d). The temperature response function for *R* is exponential, so small soil temperature anomalies can produce large *R* anomalies, especially during peak temperatures in the summer. By contrast, *GPP* is relatively insensitive to temperature except at extreme high and low temperatures (Figure 6c). The resulting temperature influence on *GPP* is very small and reflects variability in temperature extremes at high latitudes, high altitudes, and deserts. Essentially, *R* goes up and down with temperature relative to a more stable *GPP*.

LAI influences NEE inter-annual variability in tropical grasslands and high-latitude forests and tundra (Figure 6e). The LAI influence represents the indirect effect of climate (precipitation, temperature, snow cover, etc.) on plant growth, probably when the ecosystem is most sensitive, such as spring [*Houghton*, 2000]. In general, snow cover influences LAI in the high northern latitudes, temperature in the mid-latitudes, and a combination of precipitation and temperature in the tropics [*Los et al*., 2001].

Soil carbon influence is fairly evenly distributed, peaking at the equator and decreasing towards the poles (Figure 6f). Like LAI, soil carbon represents the indirect effects of climate on soil organic matter due to *GPP* anomalies. The resulting soil carbon anomalies last a year because of the assumed 1-year turnover time in the rolling respiration factor. Consequently, regions where *GPP* dominates NEE variability also show a strong soil carbon influence.

Humidity has a weak, but fairly uniform influence (Figure 6g). Transpiration during photosynthesis generally keeps the leaf surface humidity near saturation, making it insensitive to changes in ECMWF humidity (defined in the boundary layer above the canopy). Humidity influences *GPP* only when high sensible heat flux mixes relatively dry boundary layer air down into the canopy, reducing the humidity at the leaf surface and causing humidity stress.

Although globally weak, sunlight shows a fairly strong regional influence in equatorial tropical forests where persistent cloud cover reduces the light available for plant growth (Figure 6h). In SiB2, photosynthesis is light-limited only at low light levels in the early morning and late evening (sunlight below about 100 W m^{-2}). At other times, nitrogen availability or export capacity limit *GPP*. The length of time each day that *GPP* is light-limited determines the overall influence of sunlight. Precipitation anomalies change the cloud cover and incident sunlight, which determines the length of time each day when *GPP* is light-limited.

Because of the regional cancellation in the northern hemisphere, precipitation in the tropics dominates the simulated global NEE inter-annual variability. Precipitation influence on *GPP* and *R* combined account for 44% of the global NEE variability (precipitation influence on *GPP* accounts for 32% while precipitation influence on *R* accounts for 12%). Variability in LAI and soil carbon combined account for 35% of global NEE variability (23% and 12% respectively). Humidity and sunlight influences on global NEE variability are very weak (2% and 3% respectively). Temperature accounts for 16% of the global NEE inter-annual variability. The temperature influence on *GPP* is weak (1% globally). Despite dominating the northern hemisphere, regional cancellation reduces the global influence of temperature on respiration to 15% of the simulated global NEE variability. Having quantified these influences, we examined in detail two climatic phenomena known to effect inter-annual variability in temperature and precipitation: the Arctic Oscillation and the El Niño-Southern Oscillation.

5. The Arctic Oscillation and NEE Variability

The Arctic Oscillation (AO) is characterized by a north-south dipole in the strength of the zonal wind between 35°N and 55°N [*Thompson and Wallace*, 2000; *Thompson and Wallace*, 2001]. Positive AO polarity has stronger westerly winds north of 45°N and weaker winds south of 45°N, which favors increased advection of relatively warm oceanic air deep into continental interiors. Negative AO polarity has weaker mean zonal flow and more blocking, pulling cold Arctic air masses down into continental interiors. Positive AO polarity produces positive temperature anomalies over land; negative polarity produces negative anomalies. Since the AO primarily influences the northern hemisphere and since 50% of all northern hemisphere NEE anomalies occur in summer, we focused our analysis on June-July-August (JJA).

Figure 7 shows summer (JJA) correlations of air temperature and soil moisture with an AO index based on the first principle mode of sea level pressure anomalies from the NCEP reanalysis [*Thompson and Wallace*, 2000]. Figure 8 shows JJA correlations of *GPP*, *R*, and NEE with the AO index. The AO index, *GPP*, and temperature data show positive trends for 1983-93 [*Los*, 1998, *Thompson et al*. 2000], which we removed prior to correlation. We omitted correlations failing the t-test at 95% significance [*Devore*, 1995]. The degrees of freedom for the t-test are based on the total number of summer months in our simulation (assuming each month is independent). Warm air advection associated with positive AO polarity shows up as positive temperature correlations in northern Europe, Canada, and central Asia. The reduced blocking associated with positive AO polarity deceases rainfall in the same regions, resulting in negative soil moisture correlations.

Figure 8 indicates the AO signal is strongest in northern Europe for *GPP* and *R*, but competing effects and cancellation result in weak AO correlations with NEE. As seen in Figure 6, several climate factors control NEE variability in Northern Europe: temperature (via *GPP* and *R*), LAI, precipitation (via *R*), and humidity. Decreased *R* due to reduced soil moisture partially cancels increased *R* due to higher temperatures. Decreased *GPP* due to increased humidity stress partially cancels increased *GPP* due to warmer temperatures. The result is modest positive AO correlations with *R* and *GPP*. While both *GPP* and *R* increase with temperature, *R* responds more vigorously. The GPP anomalies partially cancel the *R* anomalies, resulting in weak positive NEE correlations. Similar cancellation occurs in Canada and central Asia resulting in even weaker NEE correlations with the AO. Correlations scattered throughout the southern hemisphere are probably random associations and do not reflect direct influence by the AO.

Overall, temperature effects from the AO dominate over precipitation effects. The limited spatial extent of the AO influence combined with cancellation effects result in a very weak AO signal in the NEE variability in summer. The AO can explain part of the strong temperature influence across the northern hemisphere and the Northern Europe portion of the simulated spatial pattern for NEE, but not the 2-3 year cycle in NEE variability.

6. ENSO and NEE Variability

El Niño-Southern Oscillation (ENSO) is characterized by weaker or stronger trade winds in the equatorial Pacific. Weaker trade winds (El Niño) cut off cold-water upwelling off of South America and shift the Pacific warm water pool from off Asia eastward to the central Pacific. Strong trade winds (La Niña) push the Pacific warm pool westward towards Australia. El Niño and La Niña are the extremes of alternating sea level pressures between east and west Pacific known as the Southern Oscillation. The Pacific warm pool moving with ENSO has a domino effect, shifting rainfall and temperature patterns around the globe [*Green et al*., 1997]. ENSO has a period of two to seven years. Our simulation covered two El Niño events and part of a third (1982-83, 1986-87, and 1991-92) and two La Niña events (1984-85, 1988-89).

Figure 9 shows correlations of air temperature and soil moisture with a Southern Oscillation Index (SOI) based on the sea level pressure difference between Tahiti and Darwin for 1983-93. We removed trends and omitted correlations failing the t-test at 95% significance. Negative SOI corresponds to El Niño; positive SOI corresponds to La Niña. Negative correlations mean increases during El Niño; positive correlations mean decreases during El Niño.

Rainfall patterns throughout the tropics shift as the Pacific warm pool moves east and west with ENSO. For example, rainfall (and thus soil moisture) in Australia drops during El Niño as the Pacific warm pool moves to the east, resulting in positive SOI correlations. Decreased rainfall reduces cloud cover, increases solar heating, and reduces evaporative cooling [*Kaduk and Heimann*, 1997], which increases temperature and produces negative SOI correlations. Temperature is fairly constant in the tropics, so although the correlations appear strong, the effect is small. In East Russia, reduced cloud cover associated with reduced precipitation during El Niño increases radiative cooling, decreasing temperatures and producing negative SOI correlations. In summary, ENSO primarily affects global precipitation and soil moisture patterns and weakly influences temperature.

The effects of shifting rainfall patterns on *GPP* and *R* can cancel (Figure 10). For example, in Australia and India, both *R* and *GPP* show positive correlations with SOI (both decrease as precipitation drops during El Niño). Precipitation controls NEE variability for Australia and India (Figures 6a and 6b). Areas controlled by drought stress show negative NEE correlations ($R > GPP$ during El Niño). Areas controlled by soil moisture for respiration show positive NEE correlations ($R < GPP$ during El Niño). Zero NEE correlations indicate the *R* and *GPP* anomalies cancel.

The large NEE anomaly in South America (Figure 3) results from drought stress due to rainfall shifting with ENSO. The soil water content relative to the optimum for respiration, W_{opt}, drives the spatial pattern of this anomaly. The average soil water content exceeds W_{opt} in the Amazon basin and decreases southward and westward to less than W_{opt} in the highlands of central and western South America. During El Niño, rainfall shifts from the Amazon basin and central South America to the west and southeast. The soil water in the Amazon basin decreases and respiration increases, but *GPP* is not affected, resulting negative correlations for *R* and NEE, but weak correlations for GPP. In the central South American highlands, the soil water is less than W_{opt}, so decreased rain during El Niño reduces *R* and introduces drought stress, resulting in positive *R* and *GPP* correlations. Drought stress coupled with possible problems with the ECMWF precipitation data (described above) produce a highly variable NEE anomaly, but partial cancellation between *GPP* and *R* weakens the NEE correlation with ENSO.

The ENSO influence above 30°N is weak. Temperature variability due to ENSO shows up as a strong correlation with *R* in east Russia. The high values of LAI influence on NEE variability (Figure 6g) and corresponding high soil moisture correlations indicate ENSO influences snow cover, melting times, and spring plant growth [*Kaduk and Heimann*, 1997; *Los et al*. 2001] in Europe and Canada. This may partly explain the simulated NEE anomaly pattern in the northern hemisphere. However, ENSO does not explain the strong temperature influence across the northern hemisphere or the 2-3 year cycle in NEE variability.

Overall, ENSO primarily affects NEE variability in the tropics through changes in precipitation, explaining much of the NEE variability simulated in South America, Africa, and Asia. While our correlations are statistically significant at 95% assuming each month is independent, our simulation covers only three ENSO cycles. Our results are consistent with that expected from ENSO, but a more rigorous analysis requires simulations of several decades.

7. Conclusions

The global NEE from our simulation captured the salient features of the observed global CO_2 growth rate. The detailed process information and high time resolution in SiB2 allowed us to isolate and quantify the influences of climate on global and regional inter-annual variability of NEE. Further, using remotely sensed LAI we estimated the overall influence of plant biomass on GPP variability. Assuming a 1-year turnover time we estimated the effect of below ground biomass on respiration variability. Using biome specific turnover times would improve the timing of respiration anomalies. Adding an ocean model would improve the match with the observed CO_2 growth rate. Explicitly tracking various carbon and nitrogen pools would isolate the effects of land use, growing season length, nitrogen availability, and other factors that influence NEE inter-annual variability.

The tropical grasslands in South America and Africa show the highest NEE variability. The large South American NEE anomaly is driven by shifting precipitation with ENSO, but may also result, in part, from ECMWF precipitation errors. The simulated NEE in the northern hemisphere shows a pattern of alternating positive and negative anomalies with periods of 2-3 years and amplitudes of 0.2 to 0.4 GtC yr^{-1}. The alternating anomalies tend to cancel such that the tropics control global NEE inter-annual variability while the northern hemisphere controls the global NEE seasonal cycle.

Due to cancellation and competing effects, no single climate variable controls global or regional NEE inter-annual variability. Precipitation exerts the greatest influence (44% of global NEE variability), followed by LAI (23%), temperature (16%), and soil carbon (12%). Humidity and available light do not strongly influence global NEE variability. Climate influences have strong regional differences: temperature influence on respiration dominates in the extra-tropics while precipitation influence on *GPP* and *R* dominates in the tropics. For regions controlled by precipitation the soil water content relative to W_{opt} determines whether *GPP* or *R* controls NEE variability. In dry soils ($W < W_{opt}$), *GPP* dominates; in wet soils ($W > W_{opt}$), *R* dominates.

The influence of ENSO on NEE variability is consistent with that expected for shifting precipitation patterns in the tropics, especially for the large South American anomaly. A definitive assessment requires a longer time record, since our simulation covered only 3 ENSO cycles. Except in northern Europe, temperature advection by the AO does not significantly influence NEE variability. Neither the AO nor ENSO fully explain the temperature influence on respiration or the simulated NEE anomaly pattern in the northern hemisphere.

Acknowledgments. This research was funded through the University of California at Berkeley under NASA grant SA2805-23941 and through the University of California at Santa Barbara under NASA Cooperative Agreement NCC5-302, the Earth System Science Workbench (ESSW): a scalable infrastructure for Earth Science Information Partners (ESIPs). We thank Thomas Conway of the National Oceanic and Atmospheric Administration, Climate Monitoring and Diagnostics Laboratory, Boulder, Colorado for supplying the CO_2 growth rate data. We thank David Thompson of the Atmospherics Sciences Department, Colorado State University for valuable advice and insight regarding our analysis of the Arctic Oscillation.

References

Ball, J. T., An analysis of stomatal conductance, Ph.D. Thesis, Stanford University, 1988.

Bousquet, P, P. Peylin, P. Ciais, C. Le Quéré, P. Friedlingstein, and P.Tans, Regional changes in carbon dioxide fluxes of land and oceans since 1980, *Science*, 290(5495), 1342-1346, 2000.

Conway, T. J., P. P. Tans, L. S. Waterman, K. W. Thoning, D. R. Kitzis, K. A. Masarie, and N. Zhang, Evidence for Interannual Variability of the Carbon Cycle from the National Oceanic and Atmospheric Administration/Climate Monitoring and Diagnostics Laboratory Global Air Sampling Network, *Journal of Geophysical Research*, 99(D11), 22,831-22,855, 1994.

Costa, M. H., and J. A. Foley, A Comparison of Precipitation Datasets for the Amazon Basin, *Geophysical Research Letters*, 25(2), 155-158, 1998.

Craig, S. G., K. J. Holmén, G. B. Bonan, and P. J. Rasch, Atmospheric CO_2 simulated by the National Center for Atmospheric Research Community Climate Model. 1. Mean fields and seasonal cycles, *Journal of Geophysical Research*, 13213-13235, 1998.

Defries, R. S. and J. R. G. Townshend, NDVI-derived land cover classification at a global scale, *International Journal of Remote Sensing*, 15(17), 3567-3586, 1994.

Denning, A. S., G. J. Collatz, C. Zhang, D. A. Randall, J. A. Berry, P. J. Sellers, G. D. Colello, and D. A. Dazlich, Simulations of Terrestrial Carbon Metabolism and Atmospheric CO_2 in a General Circulation Model Part 1 Surface Carbon Fluxes, *Tellus*, 48, 521-542, 1996.

Devore, J. L., Probability and Statistics for Engineering and the Sciences, Duxbury Press, 1995.

Dickinson, R. E., How coupling of the Atmosphere to ocean and Land Helps Determine the Timescales of

Inter-annual Variability of Climate, *Journal of Geophysical Research*, 105(D15), 20,115-20,119, 2000.

Fan, S. M. Gloor, J. Mahlman, S. Pacala, J. Sarmiento, T. Takahashi, and P. Tans, A large terrestrial carbon sink in North America implied by atmospheric and oceanic carbon dioxide data and models, *Science*, 282(5388), 442-446, 1998.

Fung, I., Variable Carbon Sinks, *Science*, 290, 1313, 2000.

Gibson, J. K., S. Uppala, P. Kållberg, M. Fiorino, A. Hernandez, K. Onogi, and X. Li, ECMWF 40-year Re-Analysis (ERA-40) - Archive Plans, European Centre For Medium-Range Weather Forecasts, 1999.

Goetz, S. J., S. D. Prince, J. Small, and A. C. R. Gleason, Interannual Variability of Global Terrestrial Primary Production: Results of a Model Driven with Satellite Onservations, *Journal of Geophysical Research*, 105(D15), 20,077-20,091, 2000.

Green, P.M., D. M. Legler, C. J. Miranda V, and J. J. O'Brien, The North American Climate Patterns Associated with El Nino-Southern Oscillation, Center for Ocean-Atmospheric Prediction Studies, Project Report Series 97-1, 1997.

Houghton, R. A., Interannual variability in the global carbon cycle, *Journal of Geophysical Research*, 105(D15), 20121-20130, 2000.

Houghton, R. A., E. A. Davidson, and G. M. Woodwell, Missing sinks, feedbacks, and understanding the role of terrestrial ecosystems in the global carbon balance, *Global Biogeochemical Cycles*, 12(1), 25-34, 1998.

Hunt, E. Raymond Jr., Stephen C. Piper, Ramakrishna Nemani, Charles D. Keeling, Ralf D. Otto, and Steven W. Running, Global net carbon exchange and intra-annual atmospheric CO_2 concentrations predicted by an ecosystem process model and three-dimensional atmospheric transport model, *Global Biogeochemical Cycles*, 10(3), 431-456, 1996.

Ichii, K., Y. Matsui, Y. Yamaguchi, and K. Ogawa, Comparison of Global Net Primary Production Trends Obtained From Satellite-Based Normalized Difference Vegetation Index and Carbon Cycle Model, *Global Biogeochemical Cycles*, 15(2), 351-363, 2001.

Jackson, R. B., J. Canadell, J. R. Ehleringer, H. A. Mooney, O. E. Sala, E. D. Schulze, A global analysis of root distributions for terrestrial biomes, *Oecologia* , 108, 389-411, 1996.

Kaduk, J. and M. Heimann, Assessing the Climate Sensitivity of the Global Terrestrial Carbon Cycle Model SILVAN, *Physics and Chemistry of the Earth*, 1997.

Le Quéré, C., J. C. Orr, P. Monfray, O. Aumont, and G. Madec, Interannual variability of the ocean sink of CO_2 from 1979 through 1997, *Global Biogeochemical Cycles*, 14(4), 1247-1265, 2000.

Lloyd, J., Current perspectives on the terrestrial carbon cycle, *Tellus Series B: Chemical and Physical Meteorology*, 51(2), 336-342, 1999.

Los, S. O., Linkages Between Global Vegetation and Climate: An Analysis Based on NOAA Advanced Very High Resolution Radiometer Data, Goddard Space Flight Center-1998-206852, 1998.

Los, S. O., G. J. Collatz, P. J. Sellers, C. M. Malmström, N. H. Pollack, R. S. DeFries, C. J. Tucker, L. Bounoua, M. T. Parris, and D. A. Dazlich, A global 9-year biophysical land surface dataset from NOAA AVHRR data, *Journal of Hydrometeorology*, 1(2), 183-199, 2000.

Los, S. O., G. J. Collatz, L. Bounoua, P. J. Sellers, and C. J. Tucker, Global Interannual Variations in Sea Surface Temperature and Land-Surface Vegetation, Air Temperature, and Precipitation, *Journal of Climate*, 14(7), 1535-1549, 2001.

McGuire, A. D., S. Sitch, J. S. Clein, R. Dargaville, G. Esser, J. Foley, M. Heimann, F. Foos, J. Kaplin, D. W. Kicklighter, R. A. Meier, J. M. Melillo, B. Moore III, I. C. Prentice, N. Ramankutty, T. Reichenau, A. Schloss, H. Tian, L. J. Williams, and U. Wittenburg, Carbon balance of the terrestrial biosphere in the twentieth century: Analyses of CO_2 climate and land use effects with four process-based ecosystem models, *Global Biogeochemical Cycles*, 15(1), 183-206, 2001.

Pacala, S. W., G. C. Hurtt, D. Baker, P. Peylin, R. A. Houghton, R. A. Birdsey, L. Heath, E. T. Sundquist, R. F. Stallard, P. Ciais, P. Moorcroft, J. P. Caspersen, E. Shevliakova, B. Moore, G. Kohlmaier, E. Holland, M. Gloor, M. E. Harmon, S. M. Fan, J. L. Sarmiento, C. L. Goodale, D. Schimel, and C. B. Field, Consistent land-and ocean-based U. S. carbon sink estimates, *Science*, 292, 2316-2320, 2001.

Parton, W. J., J. M. O. Scurlock, D. S. Ojima, T. G. Gilmanov, R. J. Scholes, D. S. Schimel, T. Kirchner, J-C Menaut, T. Seastedt, E. Garcia Moya, Apinan Kamnalrut, J. I. Kinyamario, Observations and modeling of biomass and soil organic matter dynamics for the grassland biome worldwide, *Global Biogeochemical Cycles*, 7(4), 785-809, 1993.

Potter, Christopher S.; Klooster, Steven A., Detecting a terrestrial biosphere sink for carbon dioxide: interannual ecosystem modeling for the mid-1980s, *Climatic Change*, 42(3), 489-503, 1999.

Potter, C. S., J. T. Randerson, C. B. Field, P. A. Matson, P. M. Vitousek, H. A. Mooney, and S. A. Klooster, Terrestrial ecosystem production: A process-oriented model based on global satellite and surface data, *Global Biogeochemical Cycles*, 7, 811-842, 1993.

Prince, S. D., S. N. Goward, S. Goetz, and K. Czajkowski, Interannual Atmosphere-Biosphere Variation: Implications for Observation and Modeling, *Journal of Geophysical Research*, 105(D15), 20,055-20,063, 2000.

Raich, J. W., and W. H. Schlesinger, The global carbon dioxide flux in soil respiration and its relationship to vegetation and climate, *Tellus Series B: Chemical and Physical Meteorology*, 44, 81-99, 1992.

Raich, J. W., E. B. Rastetter, J. M. Melillo, D. W. Kicklighter, P. A. Steudler, and B. J. Peterson, Potential Net Primary Prodution in South America: Application of a Global Model, *Ecological Applications*, 1(4), 399-429, 1991.

Randerson, J.T., M.V. Thompson, T.J. Conway, I.Y. Fung, and C.B. Field, The contribution of terrestrial sources and sinks to trends in the seasonal cycle of atmospheric carbon dioxide., *Global Biogeochemical Cycles*, 11, 535-560, 1997.

Rayner, P. J., and R. M. Law, The interannual variability of the global carbon cycle, *Tellus Series B: Chemical and Physical Meteorology*, 51(2), 210-212, 1999.

Sarmiento, J. L., Atmospheric CO_2 Stalled, *Nature*, 356, 697-698, 1993.

Sellers, P. J., C. J. Tucker, G. J. Collatz, S. O. Los, C. O. Justice, D. A. Dazlich, and D. A. Randall, A global 1° by 1° NDVI data set for climate studies, part 2: The generation of global fields of terrestrial biophysical parameters from NDVI, *International Journal of Remote Sensing*, 15(17), 3519-3545, 1994.

Sellers, P. J., D. A. Randall, G. J. Collatz, J. A. Berry, C. B. Field, D. A. Dazlich, C. Zhang, G. D. Collelo, and L. Bounoua, A Revised Land Surface Parameterization of GCMs, Part I: Model Formulation, *Journal of Climate*, 9(4), 676-705, 1996.

Sellers, P. J., S. O. Los, C. J. Tucker, C. O. Justice, D. A. Dazlich, G. J. Collatz, and D. A. Randall, A Revised Land Surface Parameterization of GCMs, Part II: The Generation of Global Fields of Terrestrial Biophysical Parameters from Satellite Data, *Journal of Climate*, 9(4), 706-737, 1996.

Sitch, S., I.C. Prentice, B. Smith, W. Cramer, J. Kaplan, W. Lucht, M. Sykes, K. Thonicke, and S. Venevsky, LPJ - A coupled model of vegetation dynamics and the terrestrial carbon cycle, The role of vegetation dynamics in the control of atmospheric CO_2 content, Ph. D. Thesis, 2000.

Tans, P. P. and D. W. R. Wallace, Carbon Cycle Research After Kyoto, *Tellus Series B: Chemical and Physical Meteorology*, 51, 562-571, 1999.

Thompson, D. W. J. and J. M. Wallace, Annular Modes in the Extratropical Circulation. Part I: Month-to-Month Variability, *Journal of Climate*, 13, 1000-1016, 2000.

Thompson, D. W. J. and J. M. Wallace, Regional Climate Impacts of the Northern Hemisphere Annular Mode, *Science*, 293, 85-89, 2001.

Thompson, D. W. J., J. M. Wallace, and G. Hegerl, Annular Modes in the Extratropical Circulation. Part II: Trends, *Journal of Climate*, 13, 1018-1036, 2000.

Tian, H. J. M. Melillo, D. W., Kicklighter, A. D. McGuire, J. V. K. Helfrich III, B. Moore, III, and C. J. Vorosmarty, Effect of interannual climate variability on carbon storage in Amazonian ecosystems, *Nature*, 396, 664-667, 1998.

Trolier, M., W. C. White, P. P. Tans, K. A. Masarie, and P. A. Gemery, Monitoring the Isotopic Composition of Atmnospheric CO_2: Measurements from the NOAA Global Air Sampling Network, *Journal of Geophysical Research*, 101(D20), 25,897-25,916, 1996.

Zhang, C., D. A. Dazlich, D. A., Randall, P. J. Sellers, A. S. Denning, Calculation of the Global Land Surface Energy, Water, and CO_2 Fluxes With an Off-line Version of SiB2, *Journal of Geophysical Research*, 101(D14), 19061-19075, 1996.

Figure 1: Global NEE vs. Time

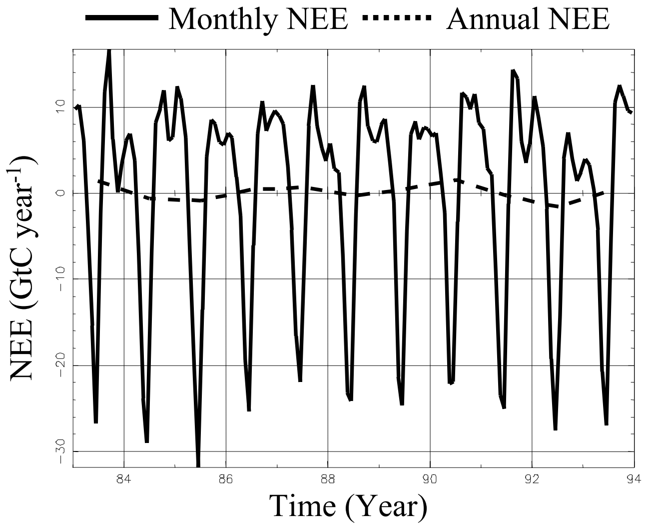

Figure 1. The Northern Hemisphere (NH) controls the seasonal changes in the simulated global NEE. Negative NEE spikes every June represent NH summer (*GPP* dominates NEE). The positive peak every September represents NH fall (respiration dominates NEE). The secondary minimum in November represents Southern Hemisphere (SH) spring. The annual NEE is near zero, but varies slightly year to year.

Figure 2: Global NEE Anomaly vs. Time

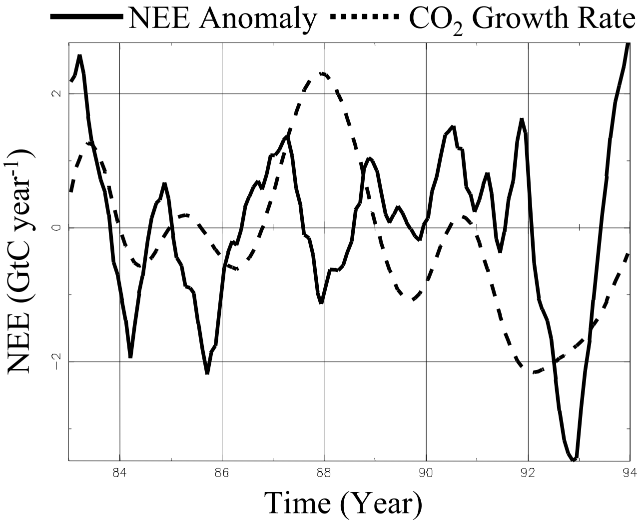

Figure 2. A 12-month running mean of the simulated global NEE anomalies captures the salient features and variability seen in anomalies of the measured global CO2 growth rate.

Figure 3: NEE Standard Deviation Map

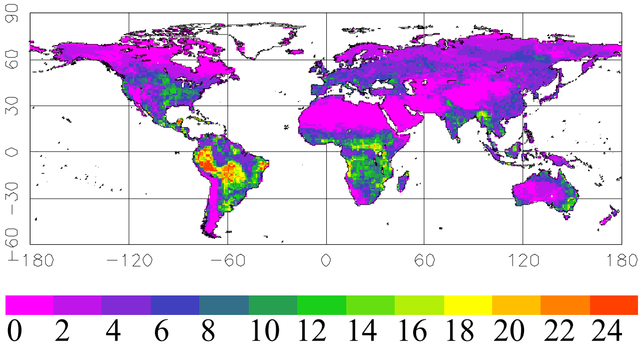

Figure 3. A map of NEE standard deviation (µg C m^{-2} s^{-1}) indicates grasslands of South America and Africa have the greatest inter-annual variability. The large anomaly in South America results from drought stress.

Figure 4: Typical NEE Anomaly Map

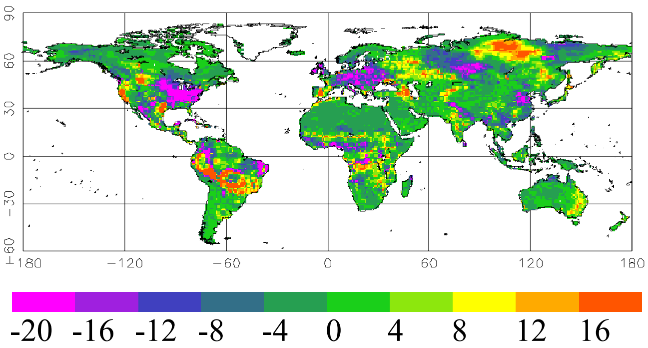

Figure 4. A map of typical simulated NEE anomalies (μg C m^{-2} s^{-1}) for July 1984 shows a pattern of alternating positive and negative regions across the northern hemisphere. These regional anomalies tend to cancel such that the tropics dominate global NEE inter-annual variability.

Figure 5: Relative Influence of R

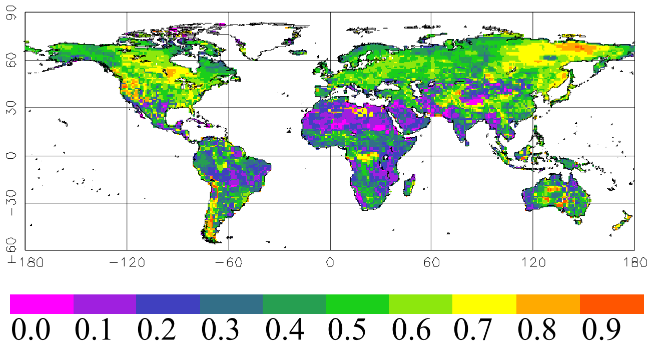

Figure 5. A map of the relative influence of respiration on NEE inter-annual variability (0 means no influence, 1 means total control) indicates respiration dominates in high latitudes. GPP and respiration exert roughly equal influence in the tropics. The relative influences of respiration and GPP are based on the relative magnitudes of their variances.

Figure 6: Relative Influence Maps

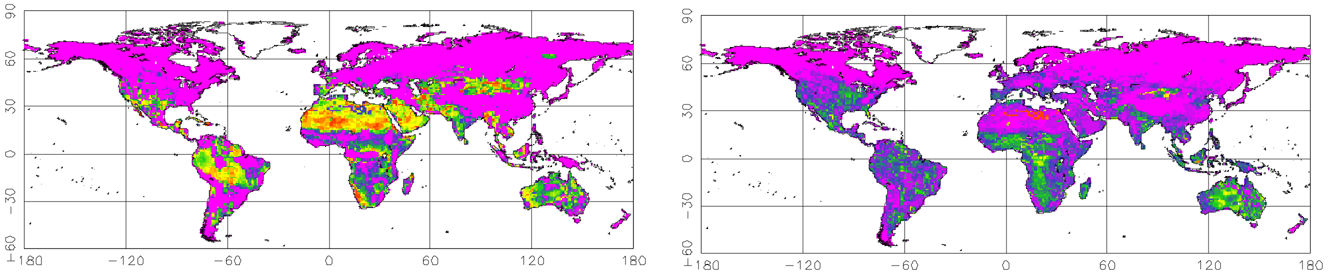
(a) Precipitation Influence on GPP

(b) Precipitation Influence on Respiration

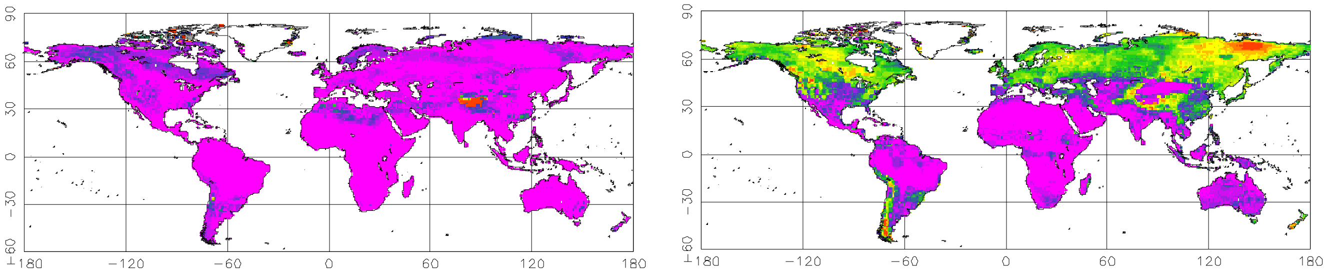
(c) Temperature Influence on GPP

(d) Temperature Influence on Respiration

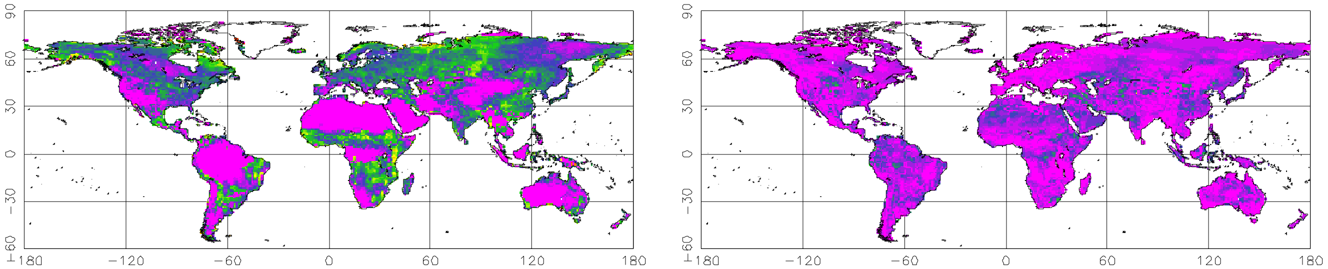
(e) Leaf Area Index Influence

(f) Soil Carbon Influence

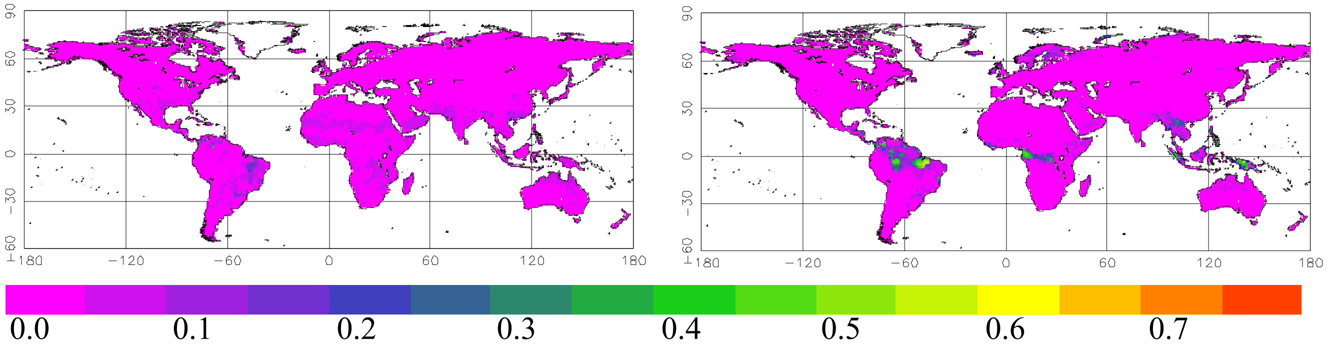
(g) Humidity Influence

(h) Light Influence

Figure 6. The relative influences of each climate factor on the simulated NEE inter-annual variability show strong regional differences. The influences are based on relative magnitudes of variance for each climate factor (0 means no influence, 1 means total control). Precipitation influence on *GPP* via soil moisture dominates in tropical grasslands and deserts. Temperature influence on respiration dominates at high latitudes. LAI influence represents climate influences during plant growth. The incident light influences NEE variability only in regions of extensive rainfall. Soil carbon has the greatest influence in the tropics. Humidity exerts a fairly uniform, but weak global influence.

Figure 7: AO-T and AO-W Correlations

(a) JJA Temperature-AO Correlations

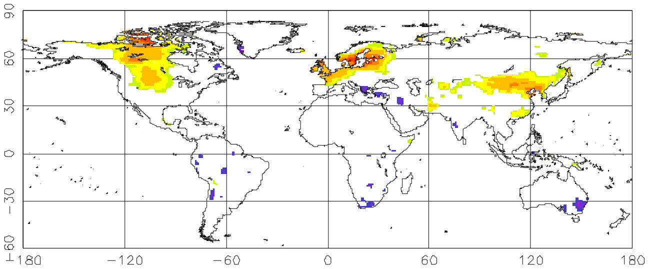

(b) JJA Soil Moisture-AO Correlations

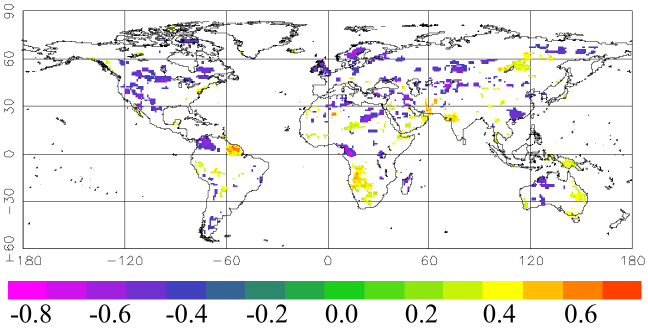

Figure 7. The Arctic Oscillation (AO) advects warm oceanic air into continental interiors, resulting in positive temperature and negative soil moisture correlations in northern Europe, central Canada and central Asia. We focused on June-July-August (JJA) because 50% of all northern hemisphere NEE anomalies occur in the summer. Southern hemisphere correlations probably do not reflect direct AO influence.

Figure 8: AO-NEE, AO-R, AO-GPP Correlations

(a) JJA NEE-AO Correlation

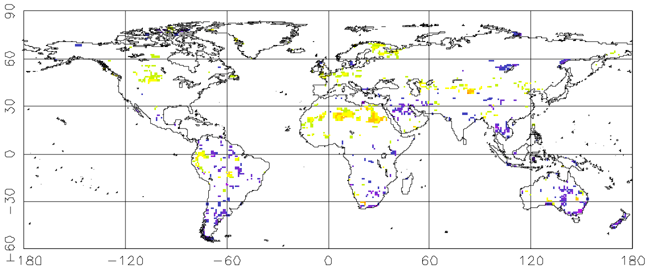

(b) JJA Respiration-AO Correlation

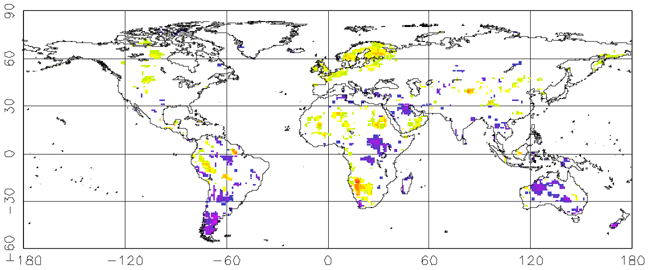

(c) JJA GPP-AO Correlation

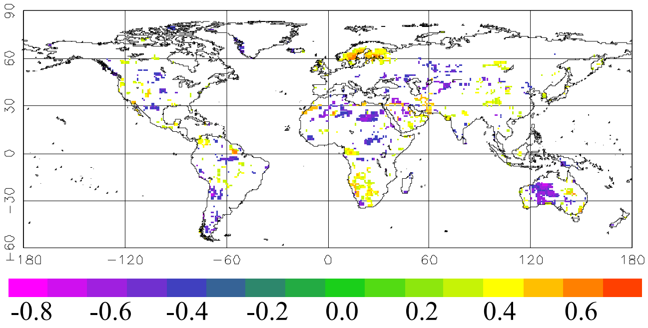

Figure 8. Respiration and GPP anomalies often cancel, resulting in very weak correlations between the Arctic Oscillation (AO) and NEE. The strongest AO signal is in Northern Europe. Southern hemisphere correlations probably do not reflect direct AO influence.

Figure 9: ENSO-T, ENSO-W Correlations

(a) Temperature-ENSO Correlations

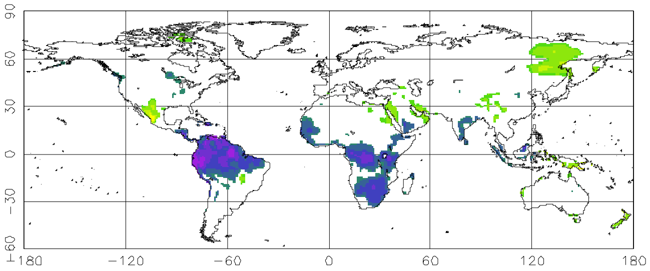

(b) Soil Moisture-ENSO Correlations

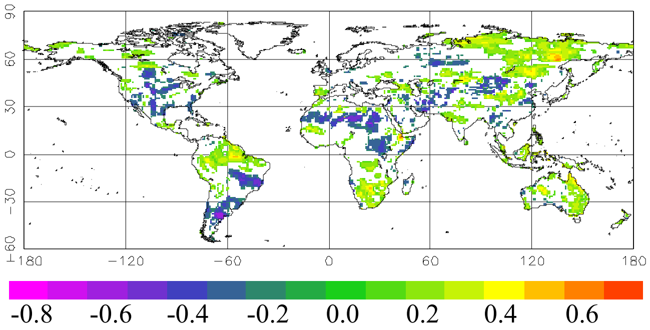

Figure 9. Correlations with a Southern Oscillation Index indicate ENSO strongly influences global precipitation patterns, especially in the tropics.

Figure 10: ENSO-T, ENSO-R, ENSO-GPP Correlations

(a) NEE-ENSO Correlation

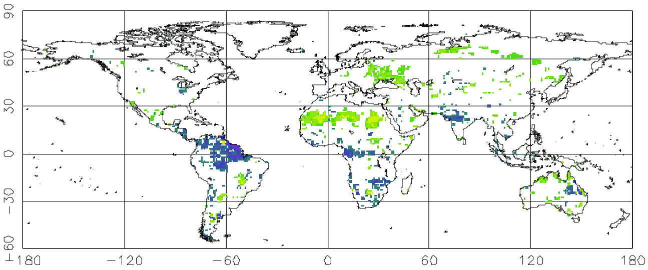

(b) Respiration- ENSO Correlation

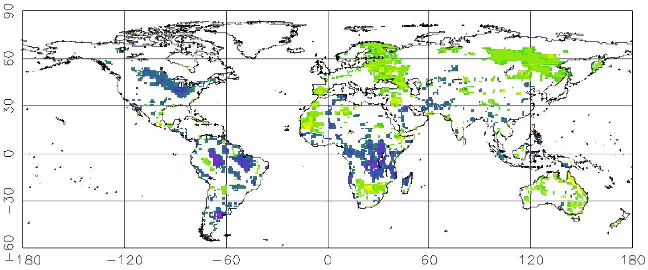

(c) GPP-ENSO Correlation

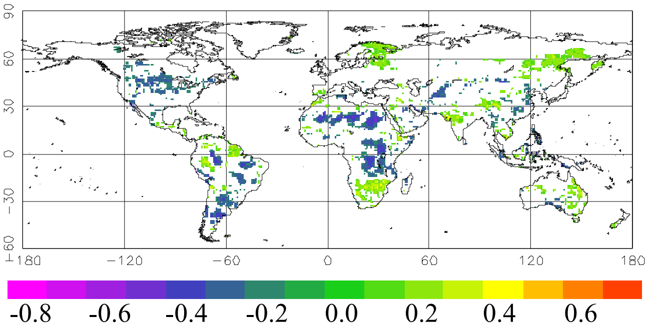

Figure 10. Correlations with a Southern Oscillation Index indicate ENSO influences NEE variability primarily in the tropics, consistent with expected shifts in precipitation.